

# Accelerating Reverse Water Gas Shift Reaction through Synergistic CO<sub>2</sub> and H<sub>2</sub> Activation on Ru–Fe–(V<sub>O</sub>-in-CeO<sub>2</sub>) Ternary Catalytic Centers

Haoyang Jiang,<sup>†</sup> Linyu Wang,<sup>†</sup> Chuanhao Wang,<sup>†</sup> Yi Xie,<sup>†</sup> Caijuan Shi, Yongcheng Xiao, Yueren Liu, Weiping Ding, and Miao Zhong\*



Cite This: *Nano Lett.* 2025, 25, 3579–3587



Read Online

## ACCESS |

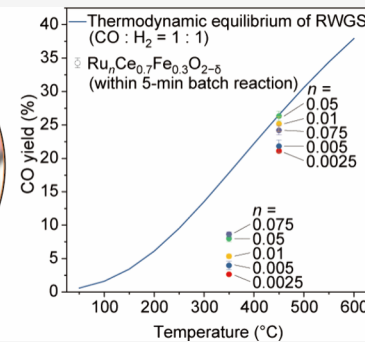
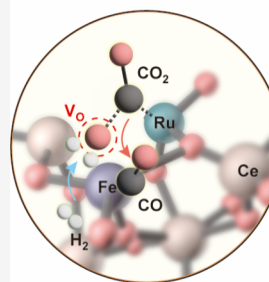
Metrics & More

Article Recommendations

Supporting Information

**ABSTRACT:** The reverse water gas shift (RWGS) reaction shows promise for converting CO<sub>2</sub> emissions to chemical feedstocks using renewable H<sub>2</sub>. However, achieving high selectivity and activity at low temperatures remains challenging due to the thermodynamically more favorable CO<sub>2</sub> methanation reaction. Here we develop a robust Ru<sub>0.0025</sub>Ce<sub>0.7</sub>Fe<sub>0.3</sub>O<sub>2-δ</sub> solid-solution nanorod catalyst featuring a ternary Fe–Ru–oxygen vacancy (V<sub>O</sub>) center, overcoming limitations in intermediate adsorption and dissociation on single-component catalysts. Incorporating a trace amount of Ru (0.25 at. %) into Ce<sub>0.7</sub>Fe<sub>0.3</sub>O<sub>2-δ</sub> markedly enhances CO<sub>2</sub> and H<sub>2</sub> dissociation and H<sub>2</sub>O formation, while the primary Ce<sub>0.7</sub>Fe<sub>0.3</sub>O<sub>2-δ</sub> solid-solution component facilitates CO desorption, lowering the RWGS onset temperature to ~200 °C. Experimental and computational analyses verify improved kinetics and stable performance with Ru<sub>0.0025</sub>Ce<sub>0.7</sub>Fe<sub>0.3</sub>O<sub>2-δ</sub>, yielding a CO production rate of 326 mmol g<sub>cat</sub><sup>-1</sup> h<sup>-1</sup>, ~100% selectivity, and a 21% yield, approaching the thermodynamic limit within a 5 min batch reaction at ~450 °C surface temperature under 300 W xenon lamp illumination.

**KEYWORDS:** Reverse water gas shift reaction, solid solution catalyst, intermediate adsorption and dissociation, reaction kinetics, H-spillover



The continuous rise in anthropogenic CO<sub>2</sub> emissions since the industrial oil era has led to various climatic and environmental challenges, such as global warming and ocean acidification.<sup>1,2</sup> Converting the greenhouse gas CO<sub>2</sub> to carbonaceous chemicals using renewable H<sub>2</sub> offers a promising CO<sub>2</sub>-utilization pathway for achieving carbon neutrality.<sup>3–7</sup> Among the various CO<sub>2</sub> hydrogenation reactions, the reverse water gas shift reaction (RWGS, CO<sub>2</sub> + H<sub>2</sub> → CO + H<sub>2</sub>O,  $\Delta H^\circ(298\text{ K}) = 42\text{ kJ mol}^{-1}$ ) stands out as a straightforward and efficient decarbonization method, producing CO—a crucial feedstock widely used in industrial processes for producing energy-rich fuels and hydrocarbons.<sup>8–10</sup> Although significant efforts have been directed toward developing efficient RWGS catalysts with a CO selectivity exceeding 90%,<sup>11–13</sup> achieving such high selectivity typically demands elevated temperatures, exceeding 500 °C,<sup>14,15</sup> which leads to substantial energy input, offsetting the benefits of large-scale implementation. In addition, the elevated temperature imposes thermodynamic constraints for direct C<sub>2+</sub> synthesis via cascade approaches and presents challenges for stable operation.<sup>16,17</sup>

The RWGS reaction necessitates a catalyst that can effectively dissociate H<sub>2</sub> to sustain a high rate of CO<sub>2</sub> reduction, while having a weak binding to CO\* to facilitate

product desorption before its further hydrogenation to produce CH<sub>4</sub>. However, catalysts with strong hydrogen dissociation capabilities typically exhibit strong CO\* binding, which inadvertently favors the exothermic CO<sub>2</sub> methanation reaction (CO<sub>2</sub> + 4H<sub>2</sub> → CH<sub>4</sub> + 2H<sub>2</sub>O,  $\Delta H^\circ(298\text{ K}) = -165\text{ kJ mol}^{-1}$ ) at low temperatures.<sup>18,19</sup> Considering these competing requirements—strong CO<sub>2</sub> and H<sub>2</sub> dissociation and weak CO\* binding—are intricately linked to the electronic structure of the catalyst,<sup>20,21</sup> achieving their simultaneous optimization in a single-component catalyst remains challenging.

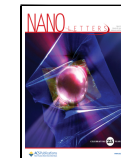
Here, we introduce an active solid-solution nanorod catalyst, Ru<sub>0.0025</sub>Ce<sub>0.7</sub>Fe<sub>0.3</sub>O<sub>2-δ</sub>, featuring a multicomponent catalytic center (Ru–Fe–(V<sub>O</sub>-in-CeO<sub>2</sub>)) that regulates intermediate dissociation and adsorption toward desired reaction at lower temperatures (Figure 1a). Specifically, the incorporation of Ru

Received: December 16, 2024

Revised: February 13, 2025

Accepted: February 13, 2025

Published: February 24, 2025



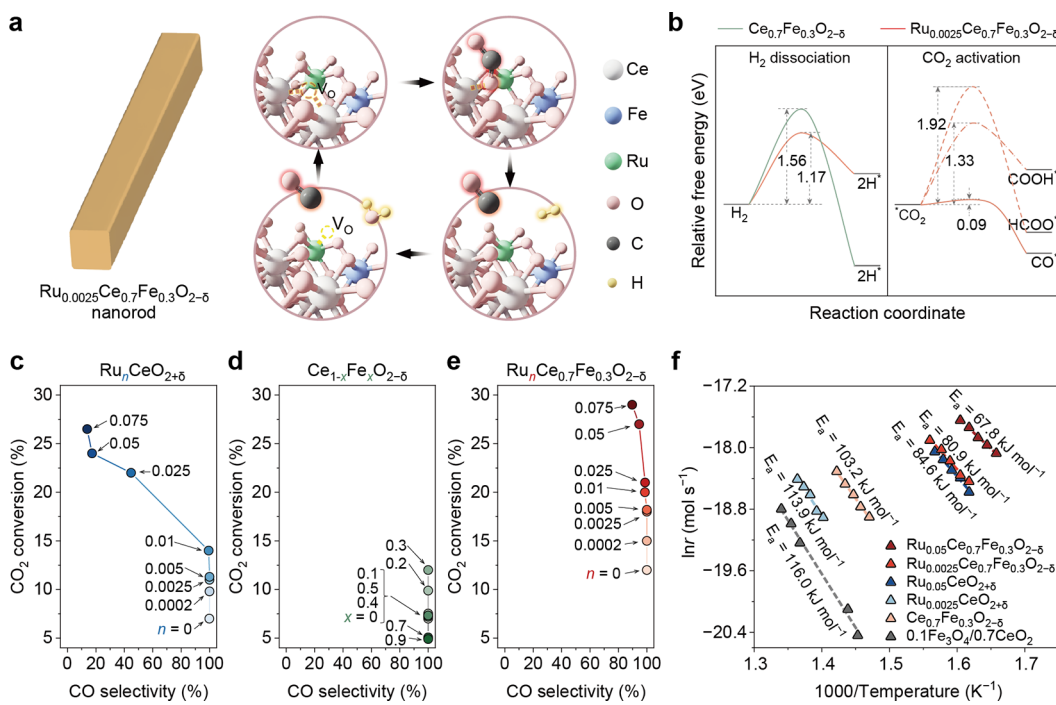


**Figure 1.** Thermocatalytic RWGS performance and proposed mechanism. (a) Illustration of Ru<sub>0.0025</sub>Ce<sub>0.7</sub>Fe<sub>0.3</sub>O<sub>2-δ</sub> nanorod catalysts, Ru-Fe-(V<sub>O</sub>-in-CeO<sub>2</sub>) ternary active centers within ceria lattice structure, and CO<sub>2</sub>-to-CO dissociative adsorption mechanism. (b) Energy barriers for H<sub>2</sub> dissociation and CO<sub>2</sub> activation on Ce<sub>0.7</sub>Fe<sub>0.3</sub>O<sub>2-δ</sub> and Ru<sub>0.0025</sub>Ce<sub>0.7</sub>Fe<sub>0.3</sub>O<sub>2-δ</sub> catalyst. (c–e) RWGS performance of the Ru<sub>n</sub>CeO<sub>2+δ</sub>, Ce<sub>1-x</sub>Fe<sub>x</sub>O<sub>2-δ</sub> and Ru<sub>n</sub>Ce<sub>0.7</sub>Fe<sub>0.3</sub>O<sub>2-δ</sub> catalysts ( $n = 0, 0.0002, 0.0025, 0.005, 0.01, 0.25, 0.05, 0.075$ ;  $x = 0, 0.1, 0.2, 0.3, 0.4, 0.5, 0.7, 0.9$ ) at a constant bulk temperature of 450 °C in a compact-type flow reactor, gas ratio: CO<sub>2</sub>/H<sub>2</sub>/Ar = 48:48:4, GHSV = 12,000 mL g<sub>cat</sub><sup>-1</sup> h<sup>-1</sup>. (f) Arrhenius plots for RWGS reactions of the 0.1Fe<sub>3</sub>O<sub>4</sub>/0.7CeO<sub>2</sub>, Ru<sub>0.0025</sub>CeO<sub>2+δ</sub>, Ce<sub>0.7</sub>Fe<sub>0.3</sub>O<sub>2-δ</sub>, Ru<sub>0.05</sub>CeO<sub>2+δ</sub>, Ru<sub>0.0025</sub>Ce<sub>0.7</sub>Fe<sub>0.3</sub>O<sub>2-δ</sub>, and Ru<sub>0.05</sub>Ce<sub>0.7</sub>Fe<sub>0.3</sub>O<sub>2-δ</sub> catalysts with external heating to different temperatures, CO<sub>2</sub>/H<sub>2</sub>/Ar = 1:4:95, GHSV = 300,000 mL g<sub>cat</sub><sup>-1</sup> h<sup>-1</sup>.

and Fe into the CeO<sub>2</sub> lattice creates abundant Ru-Fe-V<sub>O</sub> sites that facilitate dissociative CO<sub>2</sub> adsorption, where O fills the V<sub>O</sub> site with a weakly bonded CO<sup>\*</sup> on the O-filled Ru-Fe-O site, enabling prompt CO<sup>\*</sup> desorption. Simultaneously, the trace amount of Ru incorporation (0.25 at. %) in Ce<sub>0.7</sub>Fe<sub>0.3</sub>O<sub>2-δ</sub> significantly enhances H<sub>2</sub> dissociation to H, which actively reacts with surface O, regenerating V<sub>O</sub> in Ru<sub>0.0025</sub>Ce<sub>0.7</sub>Fe<sub>0.3</sub>O<sub>2-δ</sub> to facilitate CO<sub>2</sub> adsorption and completing the subsequent CO<sub>2</sub> reduction to weakly bonded CO<sup>\*</sup> on Ru-Fe-V<sub>O</sub> sites (Figure 1b). Notably, the developed Ru<sub>0.0025</sub>Ce<sub>0.7</sub>Fe<sub>0.3</sub>O<sub>2-δ</sub> solid solution enables active and selective RWGS at reduced onset temperatures (200–250 °C), surpassing single-component Ru- or Fe-incorporated catalysts. Experimental findings from the H-spillover assessment revealed that the simultaneous incorporation of Ru and Fe into CeO<sub>2</sub> is crucial for promoting H<sub>2</sub> dissociation under mild conditions (150 °C), surpassing that of their isolated components. The lower onset temperature for RWGS on Ru<sub>0.0025</sub>Ce<sub>0.7</sub>Fe<sub>0.3</sub>O<sub>2-δ</sub> is further confirmed by *in situ* infrared spectroscopic analysis and density functional theory (DFT) calculations. Arrhenius plots revealed a more than 20% reduction in the apparent activation energy with Ru<sub>0.0025</sub>Ce<sub>0.7</sub>Fe<sub>0.3</sub>O<sub>2-δ</sub> compared to those with Ce<sub>0.7</sub>Fe<sub>0.3</sub>O<sub>2-δ</sub> and Ru<sub>0.0025</sub>CeO<sub>2+δ</sub>. Our catalyst, Ru<sub>0.0025</sub>Ce<sub>0.7</sub>Fe<sub>0.3</sub>O<sub>2-δ</sub>, showed a remarkable catalytic CO production rate of 326 mmol g<sub>cat</sub><sup>-1</sup> h<sup>-1</sup> with ~100% CO selectivity in a batch reactor under 300 W xenon lamp illumination. The CO yield reached 21%, approaching the thermodynamic limit of the RWGS reaction within a short period of 5 min operation. Synchrotron X-ray scattering patterns and pair distribution function (PDF) analysis revealed stable crystallographic structure and short-

range atomic coordination for the Ru<sub>0.0025</sub>Ce<sub>0.7</sub>Fe<sub>0.3</sub>O<sub>2-δ</sub> solid solution during prolonged operation in a flow reactor at elevated temperatures. This work highlights the rational design of multicomponent catalysts, based on understanding reaction kinetics and optimizing reaction environments, and their synergy for realizing fine-tuned intermediate adsorption and dissociation toward the selective, active production in heterogeneous catalytic reactions.

The partial reducibility and abundance of oxygen vacancies in CeO<sub>2</sub> can serve as active sites for CO<sub>2</sub> activation, initiating the reverse water gas shift (RWGS) reaction with CO selectivity surpassing 90%.<sup>13,22</sup> However, the poor H<sub>2</sub> dissociation capability of pure CeO<sub>2</sub> results in low overall CO<sub>2</sub> conversion (only 7%) under the RWGS reaction conditions (CO<sub>2</sub>:H<sub>2</sub>:Ar = 48:48:4, 450 °C, and a gas hourly space-velocity (GHSV) of 12,000 mL g<sub>cat</sub><sup>-1</sup> h<sup>-1</sup>). To enhance H<sub>2</sub> dissociation, we incorporated varying amounts of Ru into CeO<sub>2</sub> (denoted as Ru<sub>n</sub>CeO<sub>2+δ</sub>,  $n = 0.0002\text{--}0.075$ , nominal values) using a hydrothermal method.<sup>23</sup> It was observed that increasing Ru incorporation led to a continuous increase in CO<sub>2</sub> conversion (Figure 1c), aligned with the expected increase in H<sub>2</sub> dissociation. However, at 2.5 at. % Ru incorporation into CeO<sub>2</sub> lattice (i.e., Ru<sub>0.025</sub>CeO<sub>2+δ</sub>), the CO selectivity evidently decreased to 55.3%, and with 5 at. % Ru incorporation (i.e., Ru<sub>0.05</sub>CeO<sub>2+δ</sub>), the reaction shifted significantly toward CH<sub>4</sub> production, with a CH<sub>4</sub> selectivity exceeding 80%. This shift in selectivity is attributed to the promoted H<sub>2</sub> dissociation which leads to an increased concentration of \*H near the Ru sites with a relatively strong CO<sup>\*</sup> binding, facilitating the over-reduction of CO<sup>\*</sup> to CH<sub>4</sub>.

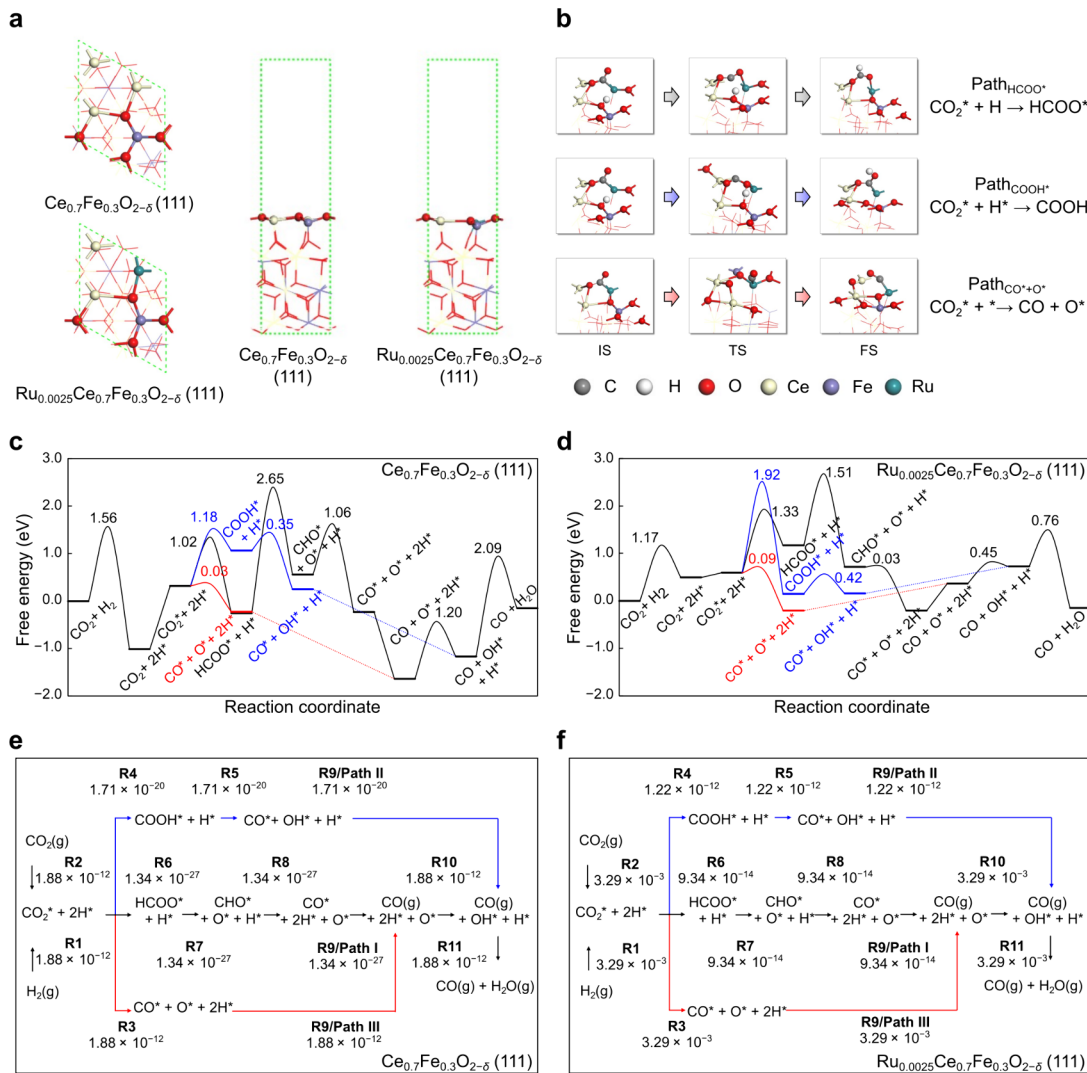


**Figure 2.** DFT calculations and microkinetic modeling for the RWGS reaction. (a) Top and side views of surface structures of the Ce<sub>0.7</sub>Fe<sub>0.3</sub>O<sub>2-δ</sub> and Ru<sub>0.0025</sub>Ce<sub>0.7</sub>Fe<sub>0.3</sub>O<sub>2-δ</sub> catalysts. (b) Initial state (IS), transition state (TS), and final state (FS) structures for CO<sub>2</sub> conversion through the three different pathways, including the hydrogenation of CO<sub>2</sub> to HCOO\* (Path<sub>HCOO\*</sub>), the hydrogenation of CO<sub>2</sub> to COOH\* (Path<sub>COOH\*</sub>), and the dissociation of CO<sub>2</sub> (Path<sub>CO\*+O\*</sub>). (c) Free energy diagram for the RWGS reaction over the Ce<sub>0.7</sub>Fe<sub>0.3</sub>O<sub>2</sub> catalyst. (d) Free energy diagram for the RWGS reaction over the Ru<sub>0.0025</sub>Ce<sub>0.7</sub>Fe<sub>0.3</sub>O<sub>2-δ</sub> catalyst. (e) Flowchart of the activity rates calculated by microkinetic modeling for the RWGS reaction over Ce<sub>0.7</sub>Fe<sub>0.3</sub>O<sub>2-δ</sub> at 723 K. (f) Flowchart of the activity rates calculated by microkinetic modeling for the RWGS reaction over Ru<sub>0.0025</sub>Ce<sub>0.7</sub>Fe<sub>0.3</sub>O<sub>2-δ</sub> at 723 K. The black, blue, and red lines correspond to the Path<sub>HCOO\*</sub>, Path<sub>COOH\*</sub>, and Path<sub>CO\*+O\*</sub> pathways, respectively. For details regarding R1–R11, refer to Tables S1 and S2.

To increase the RWGS reaction, we introduced Fe into Ru<sub>n</sub>CeO<sub>2+δ</sub> to facilitate the formation of V<sub>O</sub> while concurrently weakening the surface CO\* adsorption. Initially, we fabricated a series of Ce<sub>1-x</sub>Fe<sub>x</sub>O<sub>2-δ</sub> ( $x = 0.1\text{--}0.9$ , nominal values) solid solution nanorods using a hydrothermal method.<sup>23</sup> Ce<sub>0.7</sub>Fe<sub>0.3</sub>O<sub>2-δ</sub> was identified as the optimal composition for the RWGS reaction (Figures 1d, S1, and S2; Notes S1 and S2). Subsequently, we varied the amounts of Ru in the Ce<sub>0.7</sub>Fe<sub>0.3</sub>O<sub>2-δ</sub> solid solution to accelerate the H<sub>2</sub> dissociation, denoted as Ru<sub>n</sub>Ce<sub>0.7</sub>Fe<sub>0.3</sub>O<sub>2-δ</sub> ( $n = 0.0002\text{--}0.075$ , nominal values), and assessed the CO<sub>2</sub> hydrogenation performance of these catalysts under the same operating conditions (Figure 1e). Notably, we observed that a trace amount of Ru incorporation (0.25 atom %, i.e. Ru<sub>0.0025</sub>Ce<sub>0.7</sub>Fe<sub>0.3</sub>O<sub>2-δ</sub>) significantly improved CO<sub>2</sub> conversion to around 20%, with a CO selectivity close to unity. Even at a high Ru proportion of 7.5 at. % (i.e., Ru<sub>0.075</sub>Ce<sub>0.7</sub>Fe<sub>0.3</sub>O<sub>2-δ</sub>), the CO selectivity

remained above 90%, and the CO<sub>2</sub> conversion approached 30%. These results suggest that the formation of a new Ru<sub>n</sub>Ce<sub>x</sub>Fe<sub>1-x</sub>O<sub>2-δ</sub> solid solution efficiently weakens CO\* binding, promoting CO desorption for high CO selectivity. Simultaneously, Ru incorporation efficiently enhances the H<sub>2</sub> dissociation, accelerating the RWGS reaction.

To quantitatively analyze the impact of incorporating Ru and Fe into CeO<sub>2</sub> on the overall RWGS reaction kinetics, we conducted Arrhenius plot analyses (Note S3) with the two active catalysts of Ru<sub>0.0025</sub>Ce<sub>0.7</sub>Fe<sub>0.3</sub>O<sub>2-δ</sub> and Ru<sub>0.05</sub>Ce<sub>0.7</sub>Fe<sub>0.3</sub>O<sub>2-δ</sub> along with control catalysts of Fe<sub>3</sub>O<sub>4</sub> loaded on CeO<sub>2</sub> (Fe/(Ce+Fe) = 30 at. %, denoted as 0.1Fe<sub>3</sub>O<sub>4</sub>/0.7CeO<sub>2</sub>), Ce<sub>0.7</sub>Fe<sub>0.3</sub>O<sub>2-δ</sub>, Ru<sub>0.0025</sub>CeO<sub>2+δ</sub>, and Ru<sub>0.05</sub>CeO<sub>2+δ</sub> (Figure 1f). The results explicitly indicate that incorporating Ru into CeO<sub>2</sub> and forming the Ce<sub>0.7</sub>Fe<sub>0.3</sub>O<sub>2-δ</sub> solid solution reduces the activation energy ( $E_a$ ) of the RWGS reaction. Furthermore, the addition of a trace amount of Ru

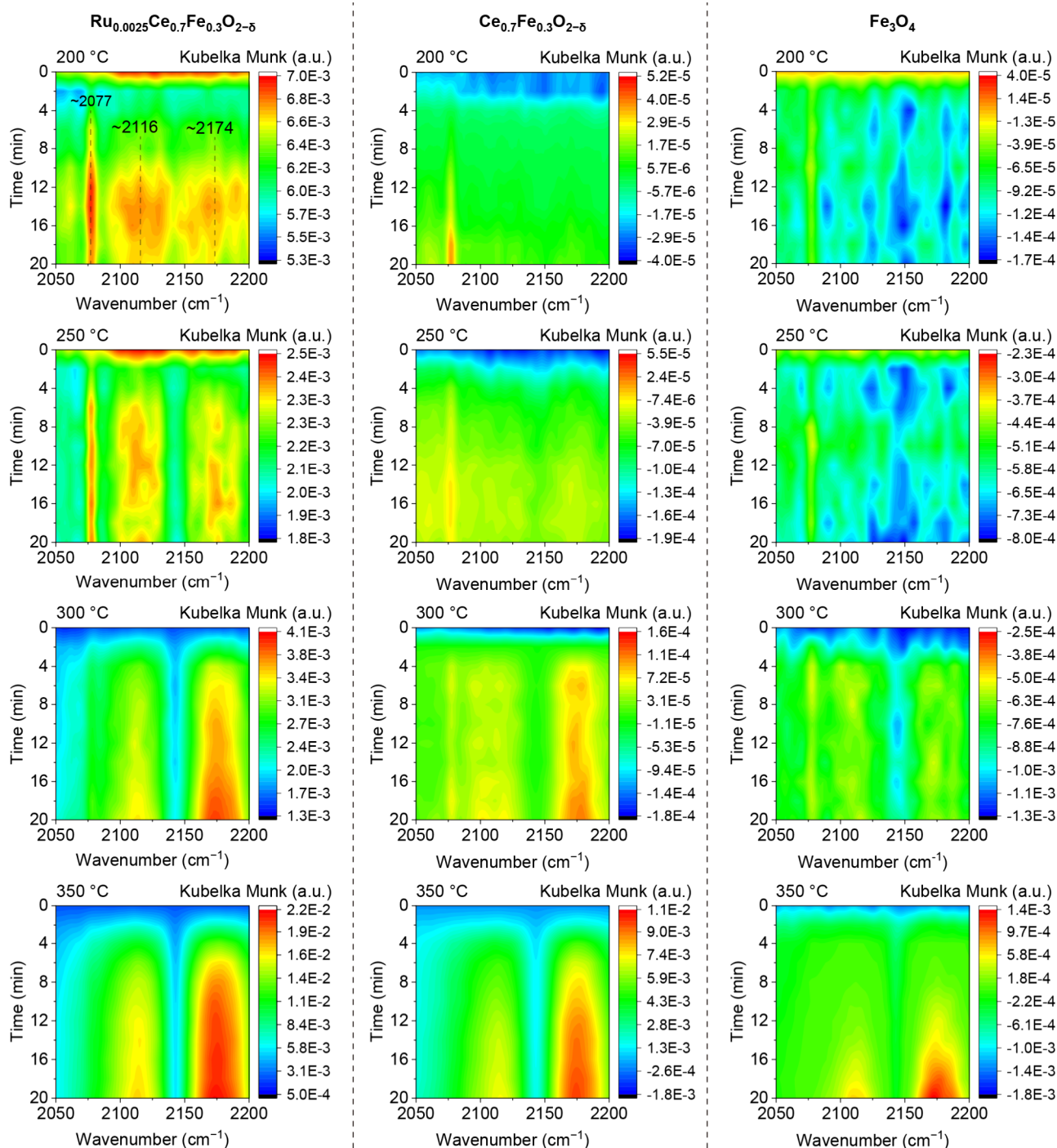


**Figure 3.** *In situ* DRIFT spectra for the  $\text{Ru}_{0.0025}\text{Ce}_{0.7}\text{Fe}_{0.3}\text{O}_{2-\delta}$ ,  $\text{Ce}_{0.7}\text{Fe}_{0.3}\text{O}_{2-\delta}$ , and  $\text{Fe}_3\text{O}_4$  catalysts at 200, 250, 300, and 350 °C in the reactant gas of 48%  $\text{CO}_2$ , 48%  $\text{H}_2$ , and 4% Ar. The DRIFT peak at  $\sim 2077 \text{ cm}^{-1}$  belongs to surface  $\text{CO}^*$ , and the two peaks at  $\sim 2174$  and  $\sim 2116 \text{ cm}^{-1}$  belong to gaseous CO. The measurements were taken every 2 min during the RWGS reaction.

(0.25 at. %) is sufficient to decrease the activation energy from 103.2  $\text{kJ mol}^{-1}$  for  $\text{Ce}_{0.7}\text{Fe}_{0.3}\text{O}_{2-\delta}$  to 80.9  $\text{kJ mol}^{-1}$ , surpassing that of 113.9  $\text{kJ mol}^{-1}$  for  $0.1\text{Fe}_3\text{O}_4/0.7\text{CeO}_2$ .

On this basis, we propose that the enhanced RWGS reaction with the  $\text{Ru}_n\text{Ce}_{0.7}\text{Fe}_{0.3}\text{O}_{2-\delta}$  solid solution catalyst stems from synergistic interactions between the  $\text{V}_\text{O}$  in  $\text{CeO}_2$  and the dopants of Ru and Fe, forming a highly active Ru–Fe– $\text{V}_\text{O}$  active center (Figure 1a). Specifically,  $\text{V}_\text{O}$  in  $\text{Ru}_n\text{Ce}_{0.7}\text{Fe}_{0.3}\text{O}_{2-\delta}$  ( $n = 0.0002\text{--}0.075$ ) facilitates  $\text{CO}_2$  adsorption. Following a dissociation pathway,  $\text{CO}^*$  is generated and departs from the

surface because of its relatively weak surface  $\text{CO}^*$  binding, leaving an O atom to fill the  $\text{V}_\text{O}$  site. Simultaneously, the Ru– $\text{Fe}$ – $\text{V}_\text{O}$  sites efficiently dissociate  $\text{H}_2$  to H. The H reacts with surface O to regenerate  $\text{V}_\text{O}$  in  $\text{Ru}_n\text{Ce}_{0.7}\text{Fe}_{0.3}\text{O}_{2-\delta}$  ( $n = 0.0002\text{--}0.075$ ), completing the RWGS reaction cycle.

To gather insights into the role of structures and active sites in  $\text{Ru}_{0.0025}\text{Ce}_{0.7}\text{Fe}_{0.3}\text{O}_{2-\delta}$  on the catalytic performance, DFT calculations were conducted (Figure 2a). Reduced terminations were established for both catalyst surfaces due to the reducing environment during activation and reaction, as

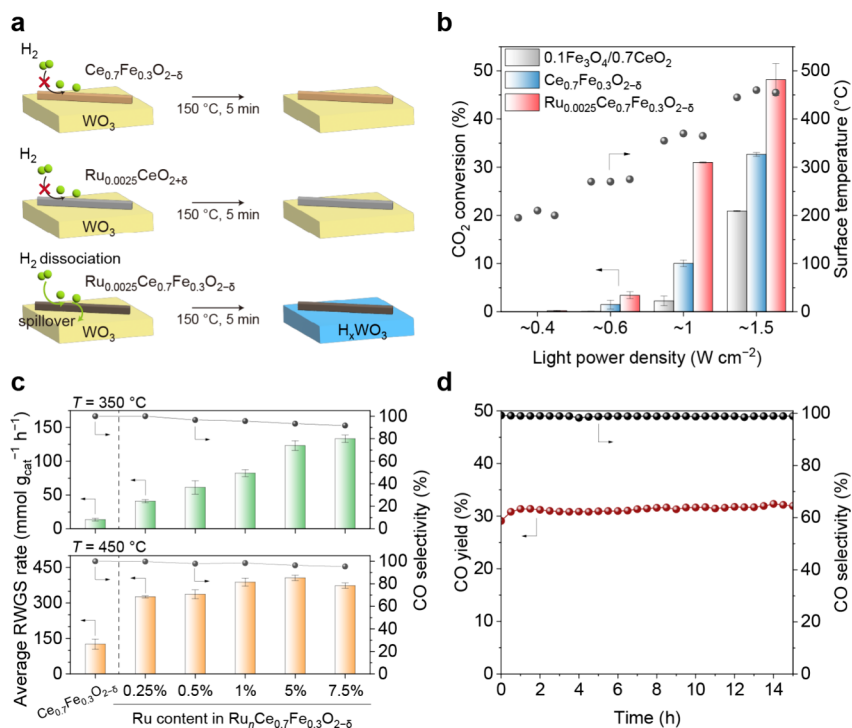


**Figure 4.** H-spillover study and catalytic performance evaluation. (a) Schematic representation of the H-spillover effect. (b) Catalytic performances of  $0.1\text{Fe}_3\text{O}_4/0.7\text{CeO}_2$ ,  $\text{Ce}_{0.7}\text{Fe}_{0.3}\text{O}_{2-\delta}$ , and  $\text{Ru}_{0.0025}\text{Ce}_{0.7}\text{Fe}_{0.3}\text{O}_{2-\delta}$  using a dilute  $\text{CO}_2$  gas in a flow reaction at different light intensities ( $\text{CO}_2/\text{H}_2/\text{Ar} = 1:4:95$ , GHSV = 36,000 mL  $\text{g}_{\text{cat}}^{-1} \text{h}^{-1}$ , 0.1 MPa) with their surface temperatures measured as plotted in the panel. (c) CO selectivity and RWGS reaction rate achieved over 5 min for the  $\text{Ce}_{0.7}\text{Fe}_{0.3}\text{O}_{2-\delta}$  and  $\text{Ru}_n\text{Ce}_{0.7}\text{Fe}_{0.3}\text{O}_{2-\delta}$  ( $n = 0.0025\text{--}0.075$ ) catalysts using concentrated  $\text{CO}_2$  gases at surface temperatures of  $\sim 350^\circ\text{C}$  and  $\sim 450^\circ\text{C}$  ( $\text{CO}_2/\text{H}_2/\text{Ar} = 48:48:4$ , 0.3 MPa). (d) Stability of  $\text{Ru}_{0.0025}\text{Ce}_{0.7}\text{Fe}_{0.3}\text{O}_{2-\delta}$  in a flow reaction system under continuous light irradiation ( $2.0 \text{ W cm}^{-2}$ ) ( $\text{CO}_2/\text{H}_2/\text{Ar}$  ratio of 48:48:4, GHSV = 12,000 mL  $\text{g}_{\text{cat}}^{-1} \text{h}^{-1}$ , 0.1 MPa). All of the reactions were performed under light irradiation without external heating. Typically, error bars represent the standard deviations from three measurements. In the case of the benchmark performance for  $\text{Ru}_{0.0025}\text{Ce}_{0.7}\text{Fe}_{0.3}\text{O}_{2-\delta}$  and  $\text{Ru}_{0.05}\text{Ce}_{0.7}\text{Fe}_{0.3}\text{O}_{2-\delta}$  at  $450^\circ\text{C}$  in panel b, the error bars represent standard deviations derived from six measurements.

confirmed by different average  $\text{V}_\text{O}$  formation free energies for  $\text{Ce}_{0.7}\text{Fe}_{0.3}\text{O}_{2-\delta}$  and  $\text{Ru}_{0.0025}\text{Ce}_{0.7}\text{Fe}_{0.3}\text{O}_{2-\delta}$  (i.e.,  $-4.49$  and  $-2.07$  eV, respectively). Three possible pathways were therefore considered for the RWGS, namely,  $\text{CO}_2$  hydrogenation to produce  $\text{HCOO}^*$  ( $\text{Path}_{\text{HCOO}^*}$ ),  $\text{CO}_2$  hydrogenation to produce  $\text{COOH}^*$  ( $\text{Path}_{\text{COOH}^*}$ ), and  $\text{CO}_2$  dissociation ( $\text{Path}_{\text{CO}^*+\text{O}^*}$ ) (Figure 2b). Based on these pathways, we calculated the free energy changes with the relevant activation barriers for the  $\text{Ce}_{0.7}\text{Fe}_{0.3}\text{O}_{2-\delta}$  and  $\text{Ru}_{0.0025}\text{Ce}_{0.7}\text{Fe}_{0.3}\text{O}_{2-\delta}$  systems (Figure 2c,d).

Upon investigation of the  $\text{H}_2$  dissociation process on both surfaces, a significantly lowered  $\text{H}_2$  dissociation energy barrier was observed with Ru incorporation (i.e., from 1.56 to 1.17 eV), indicating that  $\text{Ru}_{0.0025}\text{Ce}_{0.7}\text{Fe}_{0.3}\text{O}_{2-\delta}$  should exhibit higher activity than the  $\text{Ce}_{0.7}\text{Fe}_{0.3}\text{O}_{2-\delta}$  catalyst. Although a slightly weaker binding of  $\text{H}^*$  was found on  $\text{Ru}_{0.0025}\text{Ce}_{0.7}\text{Fe}_{0.3}\text{O}_{2-\delta}$ , the significantly shorter Ru–O bond (i.e., 2.18 Å, c.f., 2.47 Å for the Ce–O bond) reduces the geometric inhibition to promote  $\text{H}_2$  dissociation. For the conversion of  $\text{CO}_2$ , the direct dissociation of  $\text{CO}_2^*$  to  $\text{CO}^*$  and  $\text{O}^*$  was identified as the most favored pathway due to facile  $\text{CO}_2$  adsorption on the surface metal– $\text{V}_\text{O}$  sites and the lowest C=O bond cleavage energy among various competitive paths. These results indicate that hydrogenation of  $\text{O}^*$  and  $\text{OH}^*$  group is the key step in the reaction. Fortunately, the adsorption of  $\text{O}^*$  and  $\text{OH}^*$  on the stable Ru top site of  $\text{Ru}_{0.0025}\text{Ce}_{0.7}\text{Fe}_{0.3}\text{O}_{2-\delta}$  provided a relatively weak binding, decreasing the activation energy from 1.20 to 0.45 eV for

$\text{O}^*$  hydrogenation, and from 2.09 to 0.76 eV for  $\text{OH}^*$  hydrogenation. This promotes  $\text{H}_2\text{O}$  generation on  $\text{Ru}_{0.0025}\text{Ce}_{0.7}\text{Fe}_{0.3}\text{O}_{2-\delta}$  over the bare  $\text{Ce}_{0.7}\text{Fe}_{0.3}\text{O}_{2-\delta}$  catalyst. It should be noted that the reaction-limiting step of the RWGS process over  $\text{Ru}_{0.0025}\text{Ce}_{0.7}\text{Fe}_{0.3}\text{O}_{2-\delta}$  is  $\text{H}_2$  dissociation (i.e., 1.17 eV energy barrier). For comparison, the reaction-limiting step for the  $\text{Ce}_{0.7}\text{Fe}_{0.3}\text{O}_{2-\delta}$  system was  $\text{OH}^*$  hydrogenation with a significantly higher energy barrier of 2.09 eV.

Subsequently, microkinetic modeling was conducted<sup>24,25</sup> based on the established elementary steps (Tables S1 and S2) to investigate the catalytic activity of  $\text{Ru}_{0.0025}\text{Ce}_{0.7}\text{Fe}_{0.3}\text{O}_{2-\delta}$  at the molecular level (Figures 2e and 2f). More specifically, the modeling study confirmed that dissociation of  $\text{CO}_2^*$  to  $\text{CO}^*$  and  $\text{O}^*$  was predominant in the RWGS reaction. A higher reaction rate was observed for  $\text{Ru}_{0.0025}\text{Ce}_{0.7}\text{Fe}_{0.3}\text{O}_{2-\delta}$  than for  $\text{Ce}_{0.7}\text{Fe}_{0.3}\text{O}_{2-\delta}$  with turnover frequencies (TOFs) of  $3.29 \times 10^{-3} \text{ s}^{-1}$  and  $1.88 \times 10^{-12} \text{ s}^{-1}$  being determined, respectively. These results align with the onset temperatures shown in Figure S3 and Arrhenius plots presented in Figure 1f, wherein the apparent activation energy decreases from  $\sim 103 \text{ kJ mol}^{-1}$  for  $\text{Ce}_{0.7}\text{Fe}_{0.3}\text{O}_{2-\delta}$  to  $\sim 80.9 \text{ kJ mol}^{-1}$  for  $\text{Ru}_{0.0025}\text{Ce}_{0.7}\text{Fe}_{0.3}\text{O}_{2-\delta}$ .

We performed *in situ* diffuse reflectance infrared Fourier transform spectroscopy (DRIFT) experiments to explore further the reaction mechanisms of different catalysts. As shown in Figure 3, a substantial amount of adsorbed  $\text{CO}^*$  ( $\sim 2077 \text{ cm}^{-1}$ ) and desorbed gaseous CO ( $\sim 2174$  and  $\sim 2116 \text{ cm}^{-1}$ )<sup>26</sup> were observed at a low temperature of  $200^\circ\text{C}$  for  $\text{Ru}_{0.0025}\text{Ce}_{0.7}\text{Fe}_{0.3}\text{O}_{2-\delta}$ , consistent with the low RWGS onset

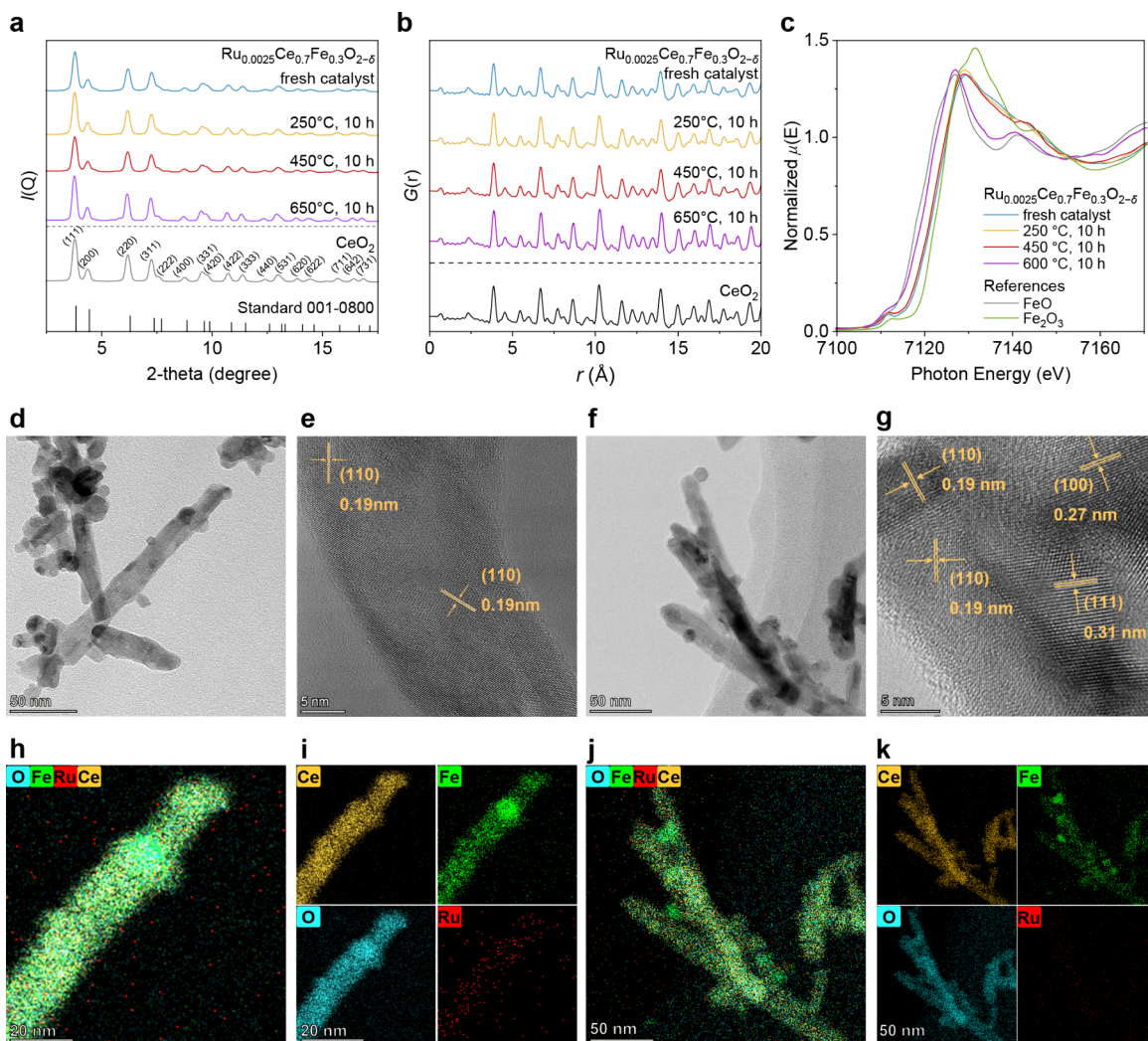


**Figure 5.** Characterization of Ru<sub>0.0025</sub>Ce<sub>0.7</sub>Fe<sub>0.3</sub>O<sub>2-δ</sub> nanorods before and after the RWGS reactions. (a and b) Synchrotron X-ray scattering patterns of the Ru<sub>0.0025</sub>Ce<sub>0.7</sub>Fe<sub>0.3</sub>O<sub>2-δ</sub> nanorods before and after 10 h RWGS reactions at 250, 450, and 600 °C. Pure CeO<sub>2</sub> is measured as a reference under identical X-ray scattering conditions. The scattering intensities  $I(Q)$  (a) and the associated pair distribution function (b) in real space. (c) The XANES spectroscopy of Fe K edges for the Ru<sub>0.0025</sub>Ce<sub>0.7</sub>Fe<sub>0.3</sub>O<sub>2-δ</sub> nanorods before and after 10 h RWGS reactions at 250, 450, and 600 °C. The K edge of the pure Fe<sub>2</sub>O<sub>3</sub> and FeO samples are recorded as references. (d–k) TEM and HRTEM images with EDX mapping of the Ru<sub>0.0025</sub>Ce<sub>0.7</sub>Fe<sub>0.3</sub>O<sub>2-δ</sub> nanorods before and after a 10 h RWGS reaction at 450 °C.

temperature in Figure S3. In contrast, distinct gaseous CO appeared at much higher temperatures of 300 °C for Ce<sub>0.7</sub>Fe<sub>0.3</sub>O<sub>2-δ</sub> and 350 °C for Fe<sub>3</sub>O<sub>4</sub>, suggesting that CO<sub>2</sub> was likely first dissociated to CO\* on the surface vacancy sites, but the insufficient capability for Ce<sub>0.7</sub>Fe<sub>0.3</sub>O<sub>2-δ</sub> and Fe<sub>3</sub>O<sub>4</sub> to dissociate H<sub>2</sub> and regenerate oxygen vacancies limited the massive conversion of CO<sub>2</sub>. A vibration peak at ~2840 cm<sup>-1</sup> was observed for Ru<sub>0.0025</sub>Ce<sub>0.7</sub>Fe<sub>0.3</sub>O<sub>2-δ</sub> at 250 °C (Figure S4), which may be attributed to formate species. Based on the previous studies on the CH<sub>4</sub> formation mechanism, we cannot exclude the possibility that the formate pathway partially contributes to the reaction.<sup>27</sup>

According to DFT calculations, the key energy-uphill steps in the RWGS process involve H, making H<sub>2</sub> dissociation crucial on catalysts. To study the H<sub>2</sub> dissociation and spillover properties with catalysts, we examined H-spillover using a WO<sub>3</sub> chromism method. Specifically, we mixed various catalysts with WO<sub>3</sub> (1:1 mass ratio) exposed to 72% H<sub>2</sub>/Ar at 150 and 200 °C for 5 min. The H-spillover-induced WO<sub>3</sub> chromism was measured using ultraviolet-visible diffuse

reflectance spectra (UV-vis-DRS), with the detailed principles and methods described in Note S4. As illustrated in Figures 4a, S5, and S6, in the case of Ce<sub>0.7</sub>Fe<sub>0.3</sub>O<sub>2-δ</sub>/WO<sub>3</sub> and Ru<sub>0.0025</sub>CeO<sub>2+δ</sub>/WO<sub>3</sub> without Ru incorporation, no significant color change occurred before and after H<sub>2</sub> treatment, indicating a relatively weak H<sub>2</sub> dissociation capability. However, as the Ru proportion increased from 1 to 5 at. % in Ru<sub>n</sub>CeO<sub>2+δ</sub>, the H-spillover-induced chromism became more pronounced, indicating that 5% Ru is sufficient to stimulate H<sub>2</sub> dissociation and spillover. Remarkably, incorporating only 0.25% Ru into Ce<sub>0.7</sub>Fe<sub>0.3</sub>O<sub>2-δ</sub> led to a significant color change in Ru<sub>0.0025</sub>Ce<sub>0.7</sub>Fe<sub>0.3</sub>O<sub>2-δ</sub>/WO<sub>3</sub> due to pronounced H-spillover. This result aligns with the DFT calculations that the Ru–Fe–V<sub>O</sub> site in Ru<sub>0.0025</sub>Ce<sub>0.7</sub>Fe<sub>0.3</sub>O<sub>2-δ</sub> reduces the H<sub>2</sub> dissociation energy, indicating that the synergistic effect of Ru and Fe sites in ceria significantly enhances H<sub>2</sub> dissociation, and even a trace amount of Ru is sufficient to achieve the desired surface H-coverage, leading to a substantial increase in RWGS kinetics.

The successful creation of the ternary reaction center allows us to apply this solid solution catalyst to photo-thermal RWGS reactions, owing to the excellent light absorption properties of the solid solution structure (Figure S7). We evaluated the photo-thermal catalytic activity of  $0.1\text{Fe}_3\text{O}_4/0.7\text{CeO}_2$ ,  $\text{Ce}_{0.7}\text{Fe}_{0.3}\text{O}_{2-\delta}$ , and  $\text{Ru}_{0.0025}\text{Ce}_{0.7}\text{Fe}_{0.3}\text{O}_{2-\delta}$  using both flow and batch reaction systems in a standard 100 mL volume. The study involves varied gas concentrations and illumination solely from a 300 W xenon lamp, utilizing photon energy as the exclusive energy source without any external heating. The surface temperatures on the catalysts upon illumination were intuitively measured by a built-in contact-type thermal couple. We first compared the RWGS performance under dilute gas conditions ( $\text{CO}_2/\text{H}_2/\text{Ar}$  ratio of 1:4:95) in a flow reactor at different light intensities and surface temperatures. At a GHSV of 36,000 mL  $\text{g}_{\text{cat}}^{-1} \text{h}^{-1}$ ,  $\text{Ru}_{0.0025}\text{Ce}_{0.7}\text{Fe}_{0.3}\text{O}_{2-\delta}$  exhibited much higher catalytic activities compared to  $\text{Ce}_{0.7}\text{Fe}_{0.3}\text{O}_{2-\delta}$  under  $\sim 0.4\text{--}1.5 \text{W cm}^{-2}$  light illumination (i.e., at the same surface temperatures of  $\sim 200\text{--}450^\circ\text{C}$  for  $0.1\text{Fe}_3\text{O}_4/0.7\text{CeO}_2$ ,  $\text{Ce}_{0.7}\text{Fe}_{0.3}\text{O}_{2-\delta}$ , and  $\text{Ru}_{0.075}\text{Ce}_{0.7}\text{Fe}_{0.3}\text{O}_{2-\delta}$  catalysts) in Figure 4b. Subsequently, we employed a concentrated gas ( $\text{CO}_2/\text{H}_2/\text{Ar}$  ratio of 48:48:4, 48:48:4, or 64:32:4) to evaluate the RWGS performance of the  $\text{Ru}_{0.0025}\text{Ce}_{0.7}\text{Fe}_{0.3}\text{O}_{2-\delta}$  catalyst at 350 and  $450^\circ\text{C}$  in a batch reactor (Figure S8a). As shown in Figure 4c, with a  $\text{CO}_2/\text{H}_2/\text{Ar}$  ratio of 48:48:4, an average CO production rate of  $41 \text{ mmol g}_{\text{cat}}^{-1} \text{ h}^{-1}$  was achieved for  $\text{Ru}_{0.0025}\text{Ce}_{0.7}\text{Fe}_{0.3}\text{O}_{2-\delta}$  under 5 min of light illumination at  $350^\circ\text{C}$ . At  $450^\circ\text{C}$ , a rate of  $326 \text{ mmol g}_{\text{cat}}^{-1} \text{ h}^{-1}$  was obtained, which corresponds to a  $\text{CO}_2$  conversion of 21% with a CO selectivity of  $\sim 100\%$ , approaching the thermodynamic equilibrium (Figure S8b). The reaction rates were 2.5–3 times higher than those of  $\text{Ce}_{0.7}\text{Fe}_{0.3}\text{O}_{2-\delta}$  without Ru incorporation. Increasing the Ru incorporation level significantly enhanced the reaction. For the  $\text{Ru}_{0.05}\text{Ce}_{0.7}\text{Fe}_{0.3}\text{O}_{2-\delta}$  catalyst, the average rate in a 5 min batch reaction was 123  $\text{mmol g}_{\text{cat}}^{-1} \text{ h}^{-1}$  at  $350^\circ\text{C}$ . At  $450^\circ\text{C}$ , the catalyst delivered a benchmark average rate of  $406 \text{ mmol g}_{\text{cat}}^{-1} \text{ h}^{-1}$ , a  $\text{CO}_2$  conversion of 26%, and a CO selectivity of 96%. We compared  $\text{Ru}_{0.0025}\text{Ce}_{0.7}\text{Fe}_{0.3}\text{O}_{2-\delta}$  with the reported catalysts, as shown in Tables S3 and S4. The  $\text{Ru}_{0.0025}\text{Ce}_{0.7}\text{Fe}_{0.3}\text{O}_{2-\delta}$  catalyst sustained a CO yield of  $\sim 27\text{--}30\%$  with a selectivity of  $\sim 100\%$  over a continuous 15 h reaction period at a GHSV of 12,000 mL  $\text{g}_{\text{cat}}^{-1} \text{ h}^{-1}$  under flow conditions with continuous light irradiation (Figure 4d). These results confirmed the active nature of  $\text{Ru}_{0.0025}\text{Ce}_{0.7}\text{Fe}_{0.3}\text{O}_{2-\delta}$  as a durable catalyst for the RWGS reaction at lowered temperatures.

Synchrotron X-ray scattering and atomic PDF analysis were conducted to investigate the long-range crystalline structure from Bragg diffraction (for  $>10 \text{ nm}$  crystals) and short-range direct spacing correlations from diffusion scattering (for  $<10 \text{ nm}$  crystals and amorphous forms)<sup>28</sup> for the  $\text{H}_2$ -activated  $\text{Ru}_{0.0025}\text{Ce}_{0.7}\text{Fe}_{0.3}\text{O}_{2-\delta}$  catalysts before and after the RWGS reaction. As shown in Figure 5a,b, no obvious change in the scattering patterns and PDFs was observed for  $\text{Ru}_{0.0025}\text{Ce}_{0.7}\text{Fe}_{0.3}\text{O}_{2-\delta}$  before and after 10 h RWGS reactions at different temperatures compared to those of pure  $\text{CeO}_2$ . This suggests that the bond structures in  $\text{Ru}_{0.0025}\text{Ce}_{0.7}\text{Fe}_{0.3}\text{O}_{2-\delta}$  solid solution were mainly maintained without noticeable precipitation of large  $\text{FeO}_x$  or Fe aggregates during the RWGS reaction. X-ray absorption near edge structure (XANES) spectra in Figure 5c showed that the chemical states of Fe in  $\text{Ru}_{0.0025}\text{Ce}_{0.7}\text{Fe}_{0.3}\text{O}_{2-\delta}$  were between  $\text{Fe}^{3+}$  and  $\text{Fe}^{2+}$  before and after RWGS reactions at temperatures of  $\leq 450^\circ\text{C}$ . At an

elevated reaction temperature of  $600^\circ\text{C}$  in a  $\text{CO}_2/\text{H}_2 = 1:1$  atmosphere, the chemical state of Fe slightly shifted to the lower energy of  $\text{Fe}^{2+}$ . Therefore, we conclude from PDF and XANES analyses that the crystallinity and short-range atomic arrangement of  $\text{Ru}_{0.0025}\text{Ce}_{0.7}\text{Fe}_{0.3}\text{O}_{2-\delta}$  were retained before and after the RWGS reaction at  $450^\circ\text{C}$ . The Fourier transformation of the Fe K-edge extended X-ray absorption fine structure spectra (EXAFS) with  $\text{Ru}_{0.0025}\text{Ce}_{0.7}\text{Fe}_{0.3}\text{O}_{2-\delta}$  samples before reaction and after 10 h of reaction at  $450^\circ\text{C}$  is shown in Figure S9. The XPS analysis results of the  $\text{Ru}_n\text{Ce}_{0.7}\text{Fe}_{0.3}\text{O}_{2-\delta}$  ( $n = 0.0025, 0.001$ ) samples exhibit weak Ru 3p and Ru 3d signals (Figure S10), with a trend of a slight shift toward lower binding energies in the Ru peak positions after the reaction at  $450^\circ\text{C}$ , while maintaining a positive oxidation state, in line with previous literature, suggesting the generation of  $\text{V}_o$ -in- $\text{CeO}_2$  near Ru sites.<sup>29</sup> The surface Ru/(Ce+Fe) atomic ratios were estimated and are presented in Table S5, revealing no obvious surface enrichment in Ru concentration. In addition, the TEM, HR-TEM, and EDX elemental mapping images shown in Figure 5d–k indicate that Ru and Fe were dispersed in the solid-solution nanorods, and no obvious morphological changes were observed following the reaction. Further material characterization and performance comparisons are discussed in the Supporting Information (Note S2, Figures S11–S16, and Tables S6 and S7).

In summary, this study demonstrates a promising strategy, wherein the active interactions within the Ru–Fe– $\text{V}_o$  active centers on the new solid-solution surface fine-tune the  $\text{CO}_2$  and  $\text{H}_2$  binding and dissociation, thereby promoting the RWGS reaction beyond the limitations of single-component catalysts. Particularly, we highlight the impact of incorporating a precise, trace amount of 0.25 atom % Ru, which modifies the local concentrations of key intermediates to promote the reactions' kinetics, enabling control over selectivity and activity in the desired pathway. By means of the Arrhenius plot, *in situ* infrared spectroscopic, H-spillover, computational, and catalytic operational studies, a 2.5–3 times enhancement in CO production rate was observed with  $\text{Ru}_{0.0025}\text{Ce}_{0.7}\text{Fe}_{0.3}\text{O}_{2-\delta}$  solid solution compared to  $\text{Ce}_{0.7}\text{Fe}_{0.3}\text{O}_{2-\delta}$  at reduced temperatures of  $\sim 275\text{--}365^\circ\text{C}$ . A high CO production rate of  $326 \text{ mmol g}_{\text{cat}}^{-1} \text{ h}^{-1}$  with  $\sim 100\%$  CO selectivity and a 21%  $\text{CO}_2$  conversion was realized within a 5 min batch reaction under 300 W xenon lamp illumination ( $450^\circ\text{C}$ ). The  $\text{Ru}_{0.0025}\text{Ce}_{0.7}\text{Fe}_{0.3}\text{O}_{2-\delta}$  solid solution catalyst was stable during extended operation in a flow reactor, as confirmed by HRTEM, STEM-EDX, and synchrotron X-ray scattering analyses. We expect that our findings in multicomponent catalyst design, optimizing intermediate binding and dissociation, and controlling reaction kinetics and environments will contribute effectively to heterogeneous catalysis and advance its practical operation.

## ■ ASSOCIATED CONTENT

### SI Supporting Information

The Supporting Information is available free of charge at <https://pubs.acs.org/doi/10.1021/acs.nanolett.4c06427>.

Experimental procedures, computation methods, and additional results and discussion (PDF)

## AUTHOR INFORMATION

### Corresponding Author

Miao Zhong – College of Engineering and Applied Sciences, National Laboratory of Solid State Microstructures, the Frontiers Science Center for Critical Earth Material Cyclings, Collaborative Innovation Center of Advanced Microstructure, Nanjing University, Nanjing 210023, China;  orcid.org/0000-0002-1253-7783; Email: [miaozhong@nju.edu.cn](mailto:miaozhong@nju.edu.cn)

### Authors

Haoyang Jiang – College of Engineering and Applied Sciences, National Laboratory of Solid State Microstructures, the Frontiers Science Center for Critical Earth Material Cyclings, Collaborative Innovation Center of Advanced Microstructure, Nanjing University, Nanjing 210023, China

Linyu Wang – College of Engineering and Applied Sciences, National Laboratory of Solid State Microstructures, the Frontiers Science Center for Critical Earth Material Cyclings, Collaborative Innovation Center of Advanced Microstructure, Nanjing University, Nanjing 210023, China

Chuanhao Wang – Hefei National Research Center for Physical Sciences at the Microscale, Department of Chemical Physics, University of Science and Technology of China, Hefei 230026, China

Yi Xie – College of Engineering and Applied Sciences, National Laboratory of Solid State Microstructures, the Frontiers Science Center for Critical Earth Material Cyclings, Collaborative Innovation Center of Advanced Microstructure, Nanjing University, Nanjing 210023, China

Caijuan Shi – Institute of High Energy Physics, Beijing Synchrotron Radiation Facility, Chinese Academy of Sciences, Beijing 100049, China

Yongcheng Xiao – College of Engineering and Applied Sciences, National Laboratory of Solid State Microstructures, the Frontiers Science Center for Critical Earth Material Cyclings, Collaborative Innovation Center of Advanced Microstructure, Nanjing University, Nanjing 210023, China

Yueren Liu – College of Engineering and Applied Sciences, National Laboratory of Solid State Microstructures, the Frontiers Science Center for Critical Earth Material Cyclings, Collaborative Innovation Center of Advanced Microstructure, Nanjing University, Nanjing 210023, China

Weiping Ding – School of Chemistry and Chemical Engineering, Nanjing University, Nanjing 210023, China;  orcid.org/0000-0002-8034-5740

Complete contact information is available at:

<https://pubs.acs.org/10.1021/acs.nanolett.4c06427>

### Author Contributions

<sup>†</sup>H. Jiang, L. Wang, C. Wang, and Y. Xie contributed equally. The manuscript was written through contributions of all authors. All authors have given approval to the final version of the manuscript.

### Notes

The authors declare no competing financial interest.

## ACKNOWLEDGMENTS

This work was supported by the National Natural Science Foundation of China (Nos. 22272078 and 22409088), the Special Fund of Jiangsu Province Carbon Peak Carbon Neutral Science and Technology Innovation Project (No. BE2023852), and the “Innovation and Entrepreneurship of

Talents Plan” of Jiangsu Province. The authors thank Dr. Chenxi Guo from SUPCON and Dr. Lirong Zheng from Beijing Synchrotron Radiation Facility for discussions and help during the study.

## REFERENCES

- (1) Kattel, S.; Liu, P.; Chen, J. G. Tuning Selectivity of CO<sub>2</sub> Hydrogenation Reactions at the Metal/Oxide Interface. *J. Am. Chem. Soc.* **2017**, *139* (29), 9739–9754.
- (2) Chen, H.; Shi, R.; Zhang, T. Nanostructured Photothermal Materials for Environmental and Catalytic Applications. *Molecules* **2021**, *26* (24), 7552.
- (3) Mateo, D.; Cerrillo, J. L.; Durini, S.; Gascon, J. Fundamentals and Applications of Photo-Thermal Catalysis. *Chem. Soc. Rev.* **2021**, *50* (3), 2173–2210.
- (4) Chen, G.; Gao, R.; Zhao, Y.; Li, Z.; Waterhouse, G. I. N.; Shi, R.; Zhao, J.; Zhang, M.; Shang, L.; Sheng, G.; Zhang, X.; Wen, X.; Wu, L.-Z.; Tung, C.-H.; Zhang, T. Alumina-Supported CoFe Alloy Catalysts Derived from Layered-Double-Hydroxide Nanosheets for Efficient Photothermal CO<sub>2</sub> Hydrogenation to Hydrocarbons. *Adv. Mater.* **2018**, *30* (3), 1704663.
- (5) Liu, Y.; Feng, H.; Yan, X.; Wang, J.; Yang, H.; Du, Y.; Hao, W. The Origin of Enhanced Photocatalytic Activities of Hydrogenated TiO<sub>2</sub> Nanoparticles. *Dalton Trans.* **2017**, *46* (32), 10694–10699.
- (6) Shoji, S.; Peng, X.; Yamaguchi, A.; Watanabe, R.; Fukuhara, C.; Cho, Y.; Yamamoto, T.; Matsumura, S.; Yu, M.-W.; Ishii, S.; Fujita, T.; Abe, H.; Miyauchi, M. Photocatalytic Uphill Conversion of Natural Gas beyond the Limitation of Thermal Reaction Systems. *Nat. Catal.* **2020**, *3* (2), 148–153.
- (7) Yu, F.; Wang, C.; Li, Y.; Ma, H.; Wang, R.; Liu, Y.; Suzuki, N.; Terashima, C.; Ohtani, B.; Ochiai, T.; Fujishima, A.; Zhang, X. Enhanced Solar Photothermal Catalysis over Solution Plasma Activated TiO<sub>2</sub>. *Adv. Sci.* **2020**, *7* (16), 2000204.
- (8) Lahijani, P.; Zainal, Z. A.; Mohammadi, M.; Mohamed, A. R. Conversion of the Greenhouse Gas CO<sub>2</sub> to the Fuel Gas CO via the Boudouard Reaction: A Review. *Renew. Sustain. Energy Rev.* **2015**, *41*, 615–632.
- (9) Wang, W.; Wang, S.; Ma, X.; Gong, J. Recent Advances in Catalytic Hydrogenation of Carbon Dioxide. *Chem. Soc. Rev.* **2011**, *40* (7), 3703–3727.
- (10) Zhao, J.; Yang, Q.; Shi, R.; Waterhouse, G. I. N.; Zhang, X.; Wu, L.-Z.; Tung, C.-H.; Zhang, T. FeO–CeO<sub>2</sub> Nanocomposites: An Efficient and Highly Selective Catalyst System for Photothermal CO<sub>2</sub> Reduction to CO. *NPG Asia Mater.* **2020**, *12* (1), 1–9.
- (11) Zakharova, A.; Iqbal, M. W.; Madadian, E.; Simakov, D. S. A. Reverse Microemulsion-Synthesized High-Surface-Area Cu/γ-Al<sub>2</sub>O<sub>3</sub> Catalyst for CO<sub>2</sub> Conversion via Reverse Water Gas Shift. *ACS Appl. Mater. Interfaces* **2022**, *14* (19), 22082–22094.
- (12) Guo, Y.; Mei, S.; Yuan, K.; Wang, D.-J.; Liu, H.-C.; Yan, C.-H.; Zhang, Y.-W. Low-Temperature CO<sub>2</sub> Methanation over CeO<sub>2</sub>-Supported Ru Single Atoms, Nanoclusters, and Nanoparticles Competitively Tuned by Strong Metal–Support Interactions and H-Spillover Effect. *ACS Catal.* **2018**, *8* (7), 6203–6215.
- (13) Liu, H.-X.; Li, S.-Q.; Wang, W.-W.; Yu, W.-Z.; Zhang, W.-J.; Ma, C.; Jia, C.-J. Partially Sintered Copper–ceria as Excellent Catalyst for the High-Temperature Reverse Water Gas Shift Reaction. *Nat. Commun.* **2022**, *13* (1), 867.
- (14) Kim, D. H.; Han, S. W.; Yoon, H. S.; Kim, Y. D. Reverse Water Gas Shift Reaction Catalyzed by Fe Nanoparticles with High Catalytic Activity and Stability. *J. Ind. Eng. Chem.* **2015**, *23*, 67–71.
- (15) Daza, Y. A.; Kuhn, J. N. CO<sub>2</sub> Conversion by Reverse Water Gas Shift Catalysis: Comparison of Catalysts, Mechanisms and Their Consequences for CO<sub>2</sub> Conversion to Liquid Fuels. *RSC Adv.* **2016**, *6* (55), 49675–49691.
- (16) Yang, G.; Xing, C.; Hirohama, W.; Jin, Y.; Zeng, C.; Suehiro, Y.; Wang, T.; Yoneyama, Y.; Tsubaki, N. Tandem Catalytic Synthesis of Light Isoparaffin from Syngas via Fischer–Tropsch Synthesis by

Newly Developed Core–Shell-like Zeolite Capsule Catalysts. *Catal. Today* **2013**, *215*, 29–35.

(17) Xu, M.; Qin, X.; Xu, Y.; Zhang, X.; Zheng, L.; Liu, J.-X.; Wang, M.; Liu, X.; Ma, D. Boosting CO Hydrogenation towards C<sub>2+</sub> Hydrocarbons over Interfacial TiO<sub>2-x</sub>/Ni Catalysts. *Nat. Commun.* **2022**, *13* (1), 6720.

(18) Wang, L.-X.; Wang, L.; Xiao, F.-S. Tuning Product Selectivity in CO<sub>2</sub> Hydrogenation over Metal-Based Catalysts. *Chem. Sci.* **2021**, *12* (44), 14660–14673.

(19) Jiang, H.; Wang, L.; Kaneko, H.; Gu, R.; Su, G.; Li, L.; Zhang, J.; Song, H.; Zhu, F.; Yamaguchi, A.; Xu, J.; Liu, F.; Miyauchi, M.; Ding, W.; Zhong, M. Light-Driven CO<sub>2</sub> Methanation over Au-Grafted Ce<sub>0.95</sub>Ru<sub>0.05</sub>O<sub>2</sub> Solid-Solution Catalysts with Activities Approaching the Thermodynamic Limit. *Nat. Catal.* **2023**, *6*, 519–530.

(20) Chen, Y.-M.; Elkind, J. L.; Armentrout, P. B. Reactions of Ru<sup>+</sup>, Rh<sup>+</sup>, Pd<sup>+</sup>, and Ag<sup>+</sup> with H<sub>2</sub>, HD, and D<sub>2</sub>. *J. Phys. Chem.* **1995**, *99* (26), 10438–10445.

(21) Zhong, M.; Tran, K.; Min, Y.; Wang, C.; Wang, Z.; Dinh, C.-T.; De Luna, P.; Yu, Z.; Rasouli, A. S.; Brodersen, P.; Sun, S.; Voznyy, O.; Tan, C.-S.; Askerka, M.; Che, F.; Liu, M.; Seifertkaldani, A.; Pang, Y.; Lo, S.-C.; Ip, A.; Ulissi, Z.; Sargent, E. H. Accelerated Discovery of CO<sub>2</sub> Electrocatalysts Using Active Machine Learning. *Nature* **2020**, *581* (7807), 178–183.

(22) Ebrahimi, P.; Kumar, A.; Khraisheh, M. A Review of CeO<sub>2</sub> Supported Catalysts for CO<sub>2</sub> Reduction to CO through the Reverse Water Gas Shift Reaction. *Catalysts* **2022**, *12* (10), 1101.

(23) Mai, H.-X.; Sun, L.-D.; Zhang, Y.-W.; Si, R.; Feng, W.; Zhang, H.-P.; Liu, H.-C.; Yan, C.-H. Shape-Selective Synthesis and Oxygen Storage Behavior of Ceria Nanopolyhedra, Nanorods, and Nanocubes. *J. Phys. Chem. B* **2005**, *109* (51), 24380–24385.

(24) Guo, C.; Tian, X.; Fu, X.; Qin, G.; Long, J.; Li, H.; Jing, H.; Zhou, Y.; Xiao, J. Computational Design of Spinel Oxides through Coverage-Dependent Screening on the Reaction Phase Diagram. *ACS Catal.* **2022**, *12* (11), 6781–6793.

(25) Chen, J.-F.; Mao, Y.; Wang, H.-F.; Hu, P. Reversibility Iteration Method for Understanding Reaction Networks and for Solving Microkinetics in Heterogeneous Catalysis. *ACS Catal.* **2016**, *6* (10), 7078–7087.

(26) Song, D.; Li, J.; Cai, Q. In Situ Diffuse Reflectance FTIR Study of CO Adsorbed on a Cobalt Catalyst Supported by Silica with Different Pore Sizes. *J. Phys. Chem. C* **2007**, *111* (51), 18970–18979.

(27) Szamosvölgyi, A.; Rajkumar, T.; Sápi, A.; Szenti, I.; Abel, M.; Gómez-Pérez, J. F.; Baán, K.; Fogarassy, Z.; Dodony, E.; Pécz, B.; Garg, S.; Kiss, J.; Kukovecz, A.; Kónya, Z. Interfacial Ni Active Sites Strike Solid Solutional Counterpart in CO<sub>2</sub> Hydrogenation. *Environ. Technol. Innov.* **2022**, *27*, No. 102747.

(28) Terban, M. W.; Billinge, S. J. L. Structural Analysis of Molecular Materials Using the Pair Distribution Function. *Chem. Rev.* **2022**, *122* (1), 1208–1272.

(29) Chen, Y.; deGlee, B.; Tang, Y.; Wang, Z.; Zhao, B.; Wei, Y.; Zhang, L.; Yoo, S.; Pei, K.; Kim, J. H.; Ding, Y.; Hu, P.; Tao, F. F.; Liu, M. A Robust Fuel Cell Operated on Nearly Dry Methane at 500 °C Enabled by Synergistic Thermal Catalysis and Electrocatalysis. *Nat. Energy* **2018**, *3* (12), 1042.